Electronic Supplementary Material (ESI) for Journal of Materials Chemistry C.
This journal is © The Royal Society of Chemistry 2017

Electronic Supplementary Material (ESI) for J. Mater. Chem. C
This journal is © The Royal Society of Chemistry 2017

Electronic Supplementary Information (ESI) for

High-Temperature Annealing Iron Microplate with Excellent Microwave Absorption Performance and its Direct Micromagnetic Analysis by Electron Holography and Lorentz Microscopy

*Wenbin You, Wen She, Zhengwang Liu, Han Bi and Renchao Che**

Laboratory of Advanced Materials, Department of Materials Science and Collabrative Innovation Center of Chemistry for Energy Materials, Fudan University, Shanghai 200438, P. R. China
* E-mail: rcche@fudan.edu.cn

S1: The details of traditional electromagnetic measurements

Preparation of samples for electromagnetic measurement: At first, as-prepared samples were added to the epoxy resin (EP) according to a weight ratio of 1: 5, and then the mixture was divided into two portion. Then, one of the portion was coated in a square aluminum substrate (180 mm × 180 mm) with a thickness of 2 mm to test the reflection loss (**Fig. S1b**). Finally, the other portion was casted in a hollow model of a coaxial cavity with dimensions of 3 mm ×7 mm × 2 mm (**Fig. S1c**) for complex permeability and permittivity tests. [1]

Electromagnetic measurements and reflection loss value calculations: The electromagnetic measurements (complex permittivity ε_r, complex permeability μ_r) were measured with a HP8510C vector network analyzer within a coaxial reflection/transmission anechoic chamber in the frequency range from 2 to 18 GHz. The reflection loss values were obtained based on the transmission line theory, expressed as the following equations: [2]

$$Z_{\text{in}} = \sqrt{\frac{\mu_r}{\varepsilon_r}} \tanh\left[-j\left(\frac{2\pi fd}{c}\right)\sqrt{\mu_r \cdot \varepsilon_r}\right]$$

$$RL(dB) = -20\log_{10}\left|(Z_{in} - 1)/(Z_{in} + 1)\right|$$

Where Z_{in} is the input impedance between the absorber and vacuum, relative complex permittivity $\varepsilon_r = \varepsilon' - j\varepsilon''$ (real part ε' and imaginary part ε'') and complex permeability $\mu_r = \mu' - j\mu''$ (real part μ' and imaginary part μ''), f is frequency of microwave through absorber, d is the thickness of the absorber coating layer, and c is the light velocity in vacuum.

S2: Detailed discussion about morphology of iron microspheres

The morphology of the as-synthesized samples was obtained by the SEM. Base on the final analysis result, it is confirmed that a series of iron with different morphologies have been successfully produced, such as flower-like, sphere-like and anomalous polyhedron (**Fig. S3**). Flower-like particles (S-1) with uniform sizes are shown in **Fig. S3a-b** (S-1). Otherwise, surface architectures assembled by regular thin sheets could be found on the microsphere, which is more remarkable in its precursor (**Fig. 1a**). In addition, the surface morphology of the other series samples can be varied by adjusting quantity of EDA. Sphere-like particles with convex/concave surfaces can be formed upon when using more quantity of EDA (**Fig. S3c-d,** S-2). With further increasing the concentration of EDA, the flower-like sphere totally transform into anomalous polyhedrons with irregular groove defects on surface architectures (**Fig. S3e-f**, S-3).

S3: Detailed discussion about the XRD patterns of iron microspheres

The crystallographic structure of the as-synthesized samples was characterized by powder XRD. **Fig. S4** shows that the XRD patterns of sphere-like samples are a typical iron without any impurities. The sharp diffraction peaks of the as-synthesized samples located at 44.7°, 65.0° and 82.3°can be well indexed to the (110), (200) and (211) planes of iron with body centered cubic structure (JCPDS no. 06-0696. No characteristic peaks due to impurities such as iron oxides and hydroxides can be found, indicating high purity of the as-prepared samples. From the XRD patterns, we can also find a decreasing tendency of FWHM values from S-1 to S-4.

S4: Detailed discussion about the electromagnetic parameters of iron microspheres

The ε′ slightly decreases with the frequency increasing in the range of 2 – 8 GHz (**Fig. S5a-c**), for highly conductive and the skin effect becomes significant in iron sample with complete crystal structure (**Fig. S4**). And that ε′ decreasing of S-1 happens in even higher frequency could be attributed to the dielectric relaxation. While the ε″ value fluctuate not apparently which represents the quite stable capability of dielectric loss. In addition, the variation both μ′ and μ″ are negligibly small (**Fig. S5a-c**), which is agreement with stabile magnetic structure in iron sphere due to rather big grain size. It is well-known that geometrical morphology and crystal structure affect dielectric loss and magnetic loss by adjust electronic and magnetic properties. The μ′ and μ″ change tendency between sample of sphere is complex for consideration of both morphology and grain. Besides, the magnetic loss induced from eddy-current loss in high frequency can't be neglected for the near constant value of $\mu''(\mu')^{-2}(f)^{-1}$ (**Fig. S5d**).

S5: Detailed discussion about microwave absorption performance of samples in preliminary experiment

Fig. S6a-c present the three-dimensional images of coating layer thickness (2-5 mm) and the applied frequency (2-18 GHz) dependence RL value of four sample. It can be found that the iron particles show excellent absorption strength and effective absorption bandwidth (< -10 dB) in frequency from 6 to 18 GHz at a rather thin coating layer (thickness as thin as 2 mm, Figure 4.e). It can be found that the maximum RL (RL_{max}) value of the flower-like microspheres is −18.5 dB at 8.05 GHz with a thickness of 2 mm (**Fig. S6a**), and the microwave response bandwidth range of it is measured to be 6.0 – 12.39 GHz. Meanwhile, sphere-like particles with defects

and anomalous polyhedrons samples display strong microwave absorption intensities (**Fig. S6b–c**) at both thin coating layer (~ 2 mm) and thick coating layer (~ 5 mm). Moreover, the strongest absorption bands locate in lower frequency range with the increase of absorber thickness, while best absorption performance (both RL_{max} value and broad effective absorption bandwidth) is mainly obtained when the coating layer is thin (~ 2 mm). The strongest absorptions of S-2 and S-3 particles reach -39.5 and -43.2 dB in the corresponding frequency values of 11.12 and 10.23 GHz, and the absorption bandwidth ranges are measured to be, 8.44 - 15.36 and 7.40 -16.67 GHz with a coating thickness of 2 mm (**Fig. S6d**). It can be deduced that the looser structure of S-1 can't provide lots of microwave absorption. Meanwhile, the losses of propagated microwaves in S-(2-3) are not only influenced by their surface morphology, but also by magnetic property change due to grain size differentness (**Fig. S4**, FWHM of XRD pattern). Therefore, the microwave absorption regulation is complex in condition of two influence factors.

S6: More discussion about Electron holography and Lorentz microscopy

Electron holography Measurements [3]: Off-axis electron holography is a powerful technique which provides quantitative information about electrostatic and magnetic fields of sample to a resolution approaching the nanometer scale under optimal conditions. The phase shift of the electron wave that has passed through a sample is sensitive to the mean inner potential and to the in-plane magnetic induction. Neglecting dynamical diffraction effects, the phase is given in one dimension by

$$\phi(x) = \left(\frac{2\pi}{\lambda}\right)\left(\frac{E + E_0}{E(E + 2E_0)}\right)\int V(x,z)\mathrm{d}z - \left(\frac{e}{\hbar}\right) \times \iint B_{\perp}(x,z)\mathrm{d}x\mathrm{d}z$$

where z is the incident beam direction, x is a direction in the plane of the sample, $B_{\perp}$ is the magnetic induction perpendicular to both x and z, V is the mean inner potential, λ is the wavelength and E and E_0 are the kinetic and rest mass energies of the incident electron, respectively.

The amplitude and the phase shift of the aberrated electron wave passes through a sample to be determined directly, rather than its intensity in electron holography. Experimentally, the amplitude and phase are obtained by extracting one 'sideband' from the Fourier transform of the hologram. This sideband is then inverse-Fourier-transformed, and the amplitude and phase of the resulting complex image wave are calculated. In this paper, we neglect the influence of thickness and electrostatic field. The phase maps determined in this experiments showed the magnetic lines of force outer of the iron samples directly.

Lorentz microscpy Measurements [4]: When the electron beam was irradiated to a magnetic sample, Lorentz force induced by the magnetic components normal to the incident beam, should deflect the electron beam. The convergence/divergence images of magnetic domain walls will be found in TEM image at defocused plane. With the help of QPt (three Lorentz micrographs (under-, in- and over-focused images) were analyzed), magnetization distribution map was achieved using the transport-of-intensity equation (TIE Eq.). TIE Eq. is as following:

$$\frac{2\pi}{\lambda}\frac{\partial I(xyz)}{\partial z} = \nabla_{xy}\left[I(xyz)\nabla_{xy}\phi(xyz)\right],$$

which was derived from Schrödinger equation under the small angle approximation when the optical wave propagates through a phase object, where I (xyz) and ϕ (xyz) stand for the intensity and phase distributions of propagating optical wave, respectively.

Since the electrostatic potential is a function of sample thickness, although it is much smaller than the high electron energy and the sample is thin enough, it should increase the noises in the phase distribution image. The thin plate was obtained by ultrathin section of iron microplate. To get an even better simulation result, TEM observations were carried out below and above the upper limit of the defocus distance (about ± 96μm). In the simulation image, color wheel and arrow are used to define magnetic domains distribution inner iron samples, and the point in the image means the direction of arrow is oriented perpendicular outward to the paper.

S7: Supplementary references

[1] Q. Liu, Q. Cao, H. Bi, C. Liang, K. Yuan, W. She, Y. Yang, R. Che, Advanced Materials, **2016**, 28, 486.

[2] R.C. Che, L.M. Peng, X.F. Duan, Q. Chen, X.L. Liang, Advanced Materials, **2004,** 16, 401.

[3] R. E. Dunin-Borkowski, M. R. Mccartney, B. Kardynal, S. S. P. Parkin, M. R. Scheinfein, D. J. Smith, Journal of Microscopy, **2000**, 200, 187.

[4] X. Z. Yu, Y. Onose, N. Kanazawa, J. H. Park, J. H. Han, Y. Matsui1, N. Nagaosa, Y. Tokura, Nature, **2010**, 465, 901.

S8: Supplementary Table S1-S2

Sample	Concentration of EDA	Temperature and time of reduction
S-1	3.0 mL	700℃, 2 h
S-2	3.4 mL	700℃, 2 h
S-3	3.8 mL	700℃, 2 h

Table S1. The reaction condition of S-1, S-2 and S-3 respectively. Other condition is same to typical experiment.

Sample	Concentration of EDA	Temperature and time of reduction
P-1	4.6 mL	700℃, 1 h
P-2	4.6 mL	700℃, 2 h
P-3	4.6 mL	700℃, 3 h

Table S2. The reaction condition of P-1, P-2 and P-3 respectively. Other condition is same to typical experiment.

S9: Supplementary Fig. S1-S9

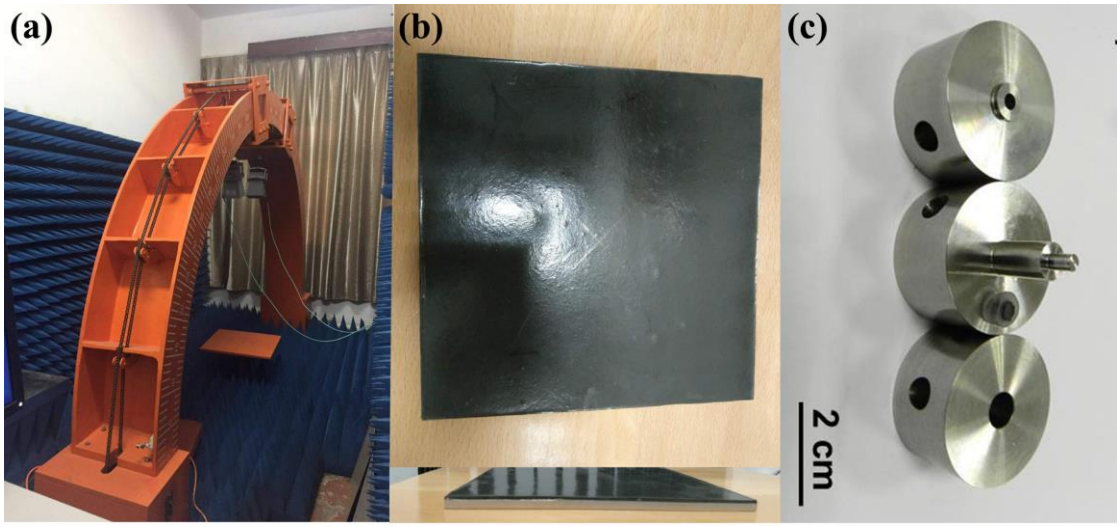

Fig. S1 (a) Photos of NRL Arch instrument, (b) vertical and side views of square aluminum substrate (180 mm x 180 mm) with 2 mm of P-3's coating and (c) model of coaxial ring method for electromagnetic measurement.

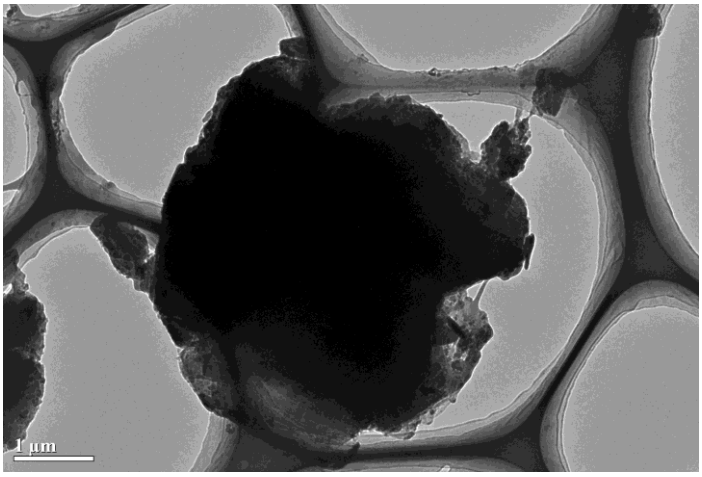

Fig. S2 TEM image of as-prepared P-1/EP after smashing the coaxial ring.

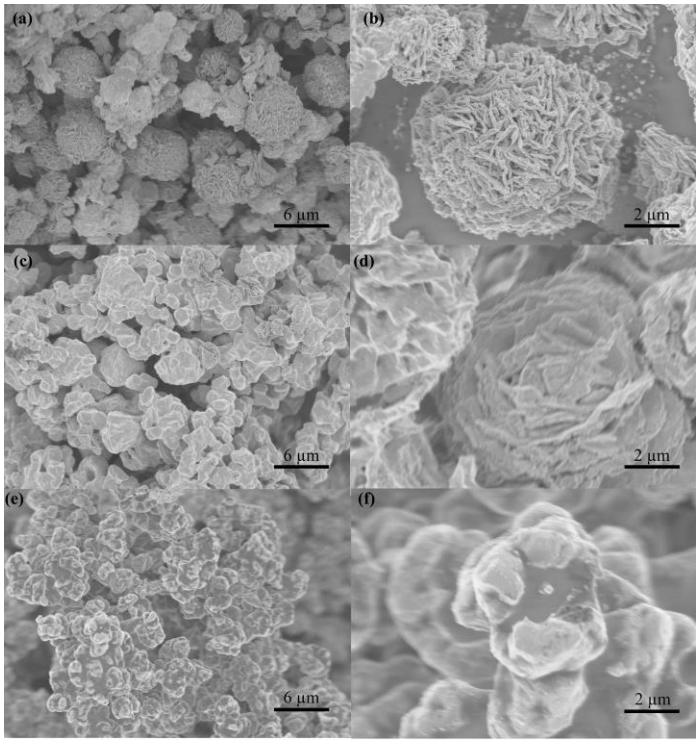

Fig. S3 SEM images of precurors after high temperture anealing, (a) S-1, (b) S-2 and (c) S-3.

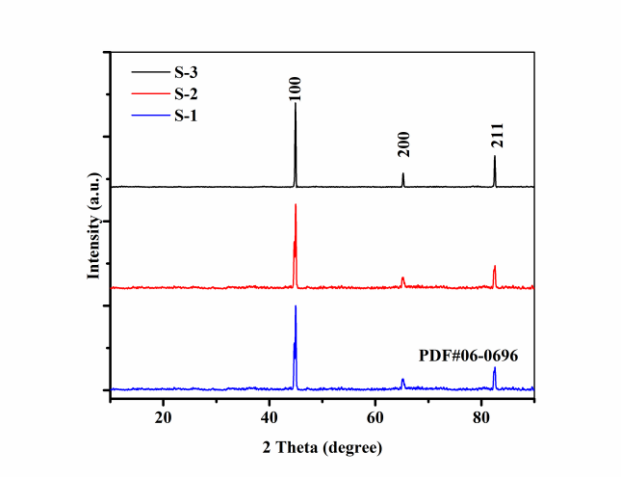

Fig. S4 XRD parterns of precurors after high temperture anealing.

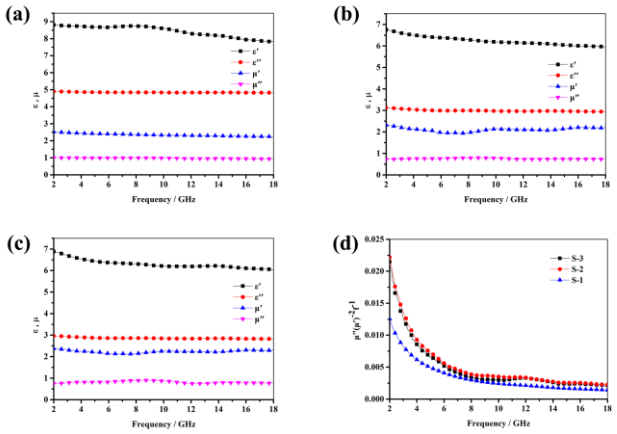

Fig. S5 (a-c) Frequency dependence of the real and imaginary parts of complex permittivity (ε) and permeability (μ) of the (a) S-1, (b) S-2 and (c) S-3; (d) $\mu''(\mu')^{-2}(f)^{-1}$ value curves of the iron microspheres. All of the parameters measured at 300K.

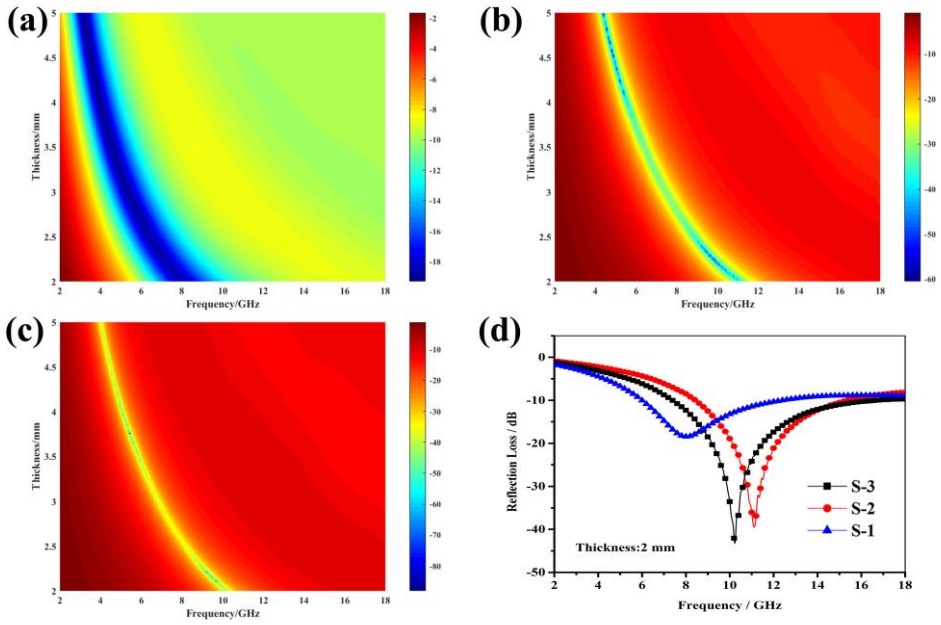

Fig. S6. (a-c) 3D representations of reflection loss (RL) values of (a) S-1, (b) S-2 and (c) S-3. (d) Frequency dependence of microwave RL curves of the iron microspheres at 2 mm thickness.

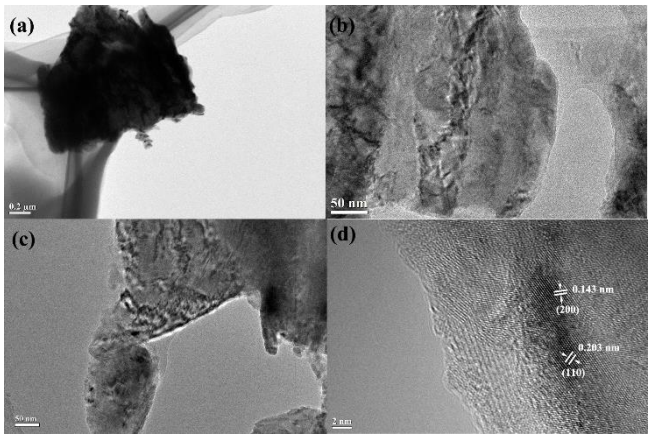

Fig. S7 (a-c) TEM images of P-3 microplates after ultrathin cutting.etching. (d) HRTEM image of P-3.

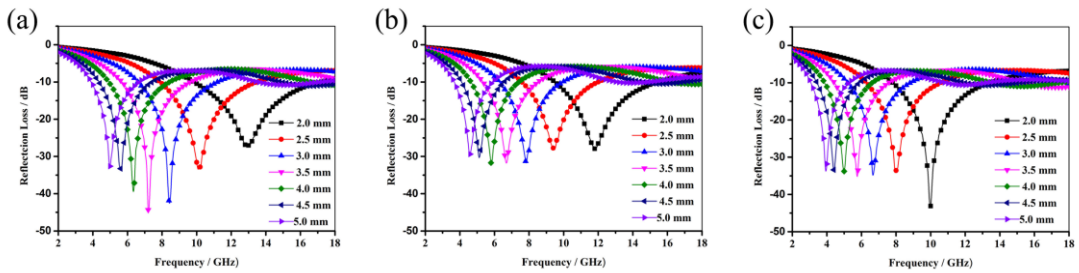

Fig. S8 Frequency dependence of microwave RL curves of the iron microplates (a) P-1, (2) P-2 and (3) P-3 with typical thicknesses (2.0 mm, 2.5 mm, 3.0 mm, 3.5 mm, 4.0 mm, 4.5 mm, 5.0 mm).

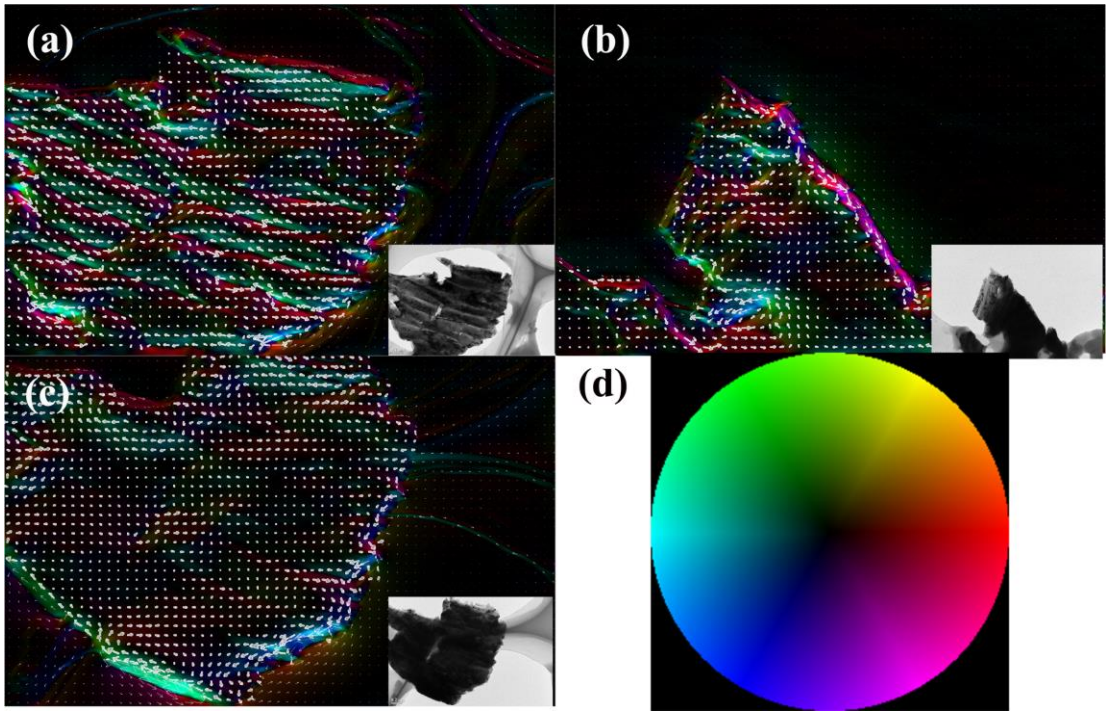

Fig. S9 (a-c) Lorentz microscopy simulation results of ultrathin section microplates (a) P-1, (b) P-2 and (c) P-3; and the insets of them show the corresponding TEM images. (d) Color wheel of above simulation graphs.